Langmuir

Article

pubs.acs.org/Langmuir

Instabilities of Layers of Deposited Molecules on Chemically Stripe Patterned Substrates: Ridges versus Drops

Christoph Honisch,[†] Te-Sheng Lin,[‡] Andreas Heuer,[§,∥,⊥] Uwe Thiele,[†,∥,⊥] and Svetlana V. Gurevich*[,†,∥,⊥]

[†]Institute for Theoretical Physics, University of Münster, Wilhelm-Klemm-Str. 9, 48149 Münster, Germany

[‡]Department of Applied Mathematics, National Chiao Tung University, Hsinchu, 30010 Taiwan

[§]Institute for Physical Chemistry, University of Münster, Correnstrasse 28/30, 48149 Münster, Germany

[∥]Center of Nonlinear Science (CeNoS), University of Münster, Corrensstrasse 2, 48149 Münster, Germany

[⊥]Center for Multiscale Theory and Computation(CMTC), University of Münster, Corrensstrasse 40, 48149 Münster, Germany

Supporting Information

ABSTRACT: A mesoscopic continuum model is employed to analyze the transport mechanisms and structure formation during the redistribution stage of deposition experiments where organic molecules are deposited on a solid substrate with periodic stripe-like wettability patterns. Transversally invariant ridges located on the more wettable stripes are identified as very important transient states and their linear stability is analyzed accompanied by direct numerical simulations of the fully nonlinear evolution equation for two-dimensional substrates. It is found that there exist two different instability modes that lead to different nonlinear evolutions that result (i) at large ridge volume in the formation of bulges that spill from the more wettable stripes onto the less wettable bare substrate and (ii) at small ridge volume in the formation of small droplets located on the more wettable stripes. In addition, the influence of different transport mechanisms during redistribution is investigated focusing on the cases of convective transport with no-slip at the substrate, transport via diffusion in the film bulk and via diffusion at the film surface. In particular, it is shown that the transport process does neither influence the linear stability thresholds nor the sequence of morphologies observed in the time simulation, but only the ratio of the time scales of the different process phases.

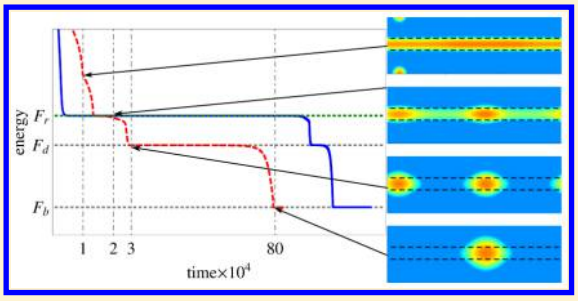

1. INTRODUCTION

Many coating and surface growth processes through which a solid substrate is covered by homogeneous or structured layers of the same or other materials combine deposition and redistribution stages that might occur successively or in parallel. Prominent examples are various homo- and heteroepitaxial surface growth processes where the redistribution of material on the substrate occurs through diffusion of deposited atoms or molecules on the surface of the substrate.[1,2] Often, the material is first deposited, e.g., via vapor deposition,[3] molecular beam deposition,[4] or (pulsed) laser deposition.[5] Then the adsorbed molecules diffuse along the surface and form two-dimensional aggregates, complete mono- or multilayers, and three-dimensional nanoscale structures like pyramids, holes, and mounds—the latter are sometimes called quantum dots and wells.[6,7]

Another example is spin-coating, where first a drop of liquid is deposited on the substrate, before convective motion caused by fast spinning of the substrate spreads the liquid into a thin film.[8,9] In the case of solutions or suspensions, the spin coating process is often accompanied by solvent evaporation and the final coating is a homogeneous or structured layer of the dried-in solute.[10−12] Another example are dip-coating and related processes where a liquid is transferred from a bath or other reservoir onto the substrate.[13,14] These examples all involve a wet stage where hydrodynamic flows caused by external forces, wettability, and capillarity are important for the redistribution of the material.[15] The flows during the wet stage may be described employing, e.g., asymptotic models as obtained via long-wave expansions from the basic equations of hydrodynamics.[16]

Many of the studied systems involve homogeneous substrates. However, there is also a growing number of experimental and theoretical studies that investigate the use of heterogeneous substrates to control the structure of deposits. Examples include recent deposition experiments with organic molecules performed by Wang et al.[17,18] on silicon oxide substrates with gold stripes, the study of dip-coating for chemically micropatterned surfaces[19] or dewetting of thin silicon films on nanopatterns formed by electron beam lithography.[20] For the growth of quantum dots on heterogeneous substrates, see ref 21.

Static morphologies emerging from capillary and wettability influences on heterogeneous substrates of various geometries are already studied in depth; however, studies of the involved

Received: June 30, 2015
Revised: September 3, 2015
Published: September 4, 2015

DOI: 10.1021/acs.langmuir.5b02407
Langmuir 2015, 31, 10618−10631

dynamics are less frequent: Morphological transitions of transversally invariant liquid ridges on two-dimensional striped substrates (i.e., mathematically equivalent to drops on one-dimensional heterogeneous substrates) were studied via minimization of macroscopic interfacial free energies in ref 22 and through bifurcation studies employing mesoscopic free energies (interface Hamiltonians) and time simulations of gradient dynamics on these energies (equivalent to long-wave hydrodynamic models) in refs 23 and 24. In these studies nonvolatile liquids are considered, i.e., liquid volume and heterogeneity properties are the main control parameters. Related steady (one-dimensional) results are obtained in studies of morphological transitions of wetting films on striped substrates.[25,26] There, the main control parameters are temperature and chemical potential, i.e., the volume of deposited liquid is a dependent quantity in this grand canonical studies. The dynamics of nanodroplets near chemical heterogeneities are investigated in ref 27.

Fully two-dimensional situations are also studied: ref 24 investigates the linear instability modes and their time scales for transversally invariant liquid ridges on homogeneous and heterogeneous (striped) substrates. In particular, they study transversal instabilities (Plateau−Rayleigh instability) and their coupling to coarsening instabilities, while ref 28 also considers the coupling to depinning modes under lateral driving and the bifurcation structure for steady two-dimensional states (i.e., height profiles depend on both substrate dimensions). The Plateau−Rayleigh instability is also considered in ref 29 together with the effect of a body force along the ridge. Sharma et al. present time simulations of dewetting dynamics for one-dimensional heterogeneous substrates and two-dimensional substrates with a less wettable square patch,[30] with stripes[31] and other two-dimensional wettability patterns.[32] Droplet spreading on patterned substrates is also considered.[33]

Most of the mentioned studies that involve two-dimensional substrates employ mesoscopic long-wave models (i.e., small gradient expansions), while refs 34 and 35 determine steady surface profiles and their stability on the basis of macroscopic interfacial free energies (note that this does not allow for a calculation of the time scales of the instabilities as they result from a balance of dissipation mechanisms and decrease in free energy). Similar results for morphological transitions on substrates with microgrooves are compared with experiments in ref 36. Other experiments concern the pattern-directed dewetting of ultrathin polymer films that results, e.g., in rows of drops.[37] The dewetting of volatile octane films on substrates with alternating completely and partially wettable stripes is experimentally studied in ref 38 and compared to steady profiles obtained through minimization of an interface Hamiltonian. Macroscopic experiments with water on chemically heterogeneous substrates are reported in ref 39. Part of these works are reviewed in ref 40.

The present study is directly motivated by deposition experiments with organic molcules performed by Wang et al.[17,18] Several types of light-emitting organic molecules (e.g., diferrocene (DiFc); 1,6- Bis(2-hydroxyphenol)pyridinel boron bis(4-*n*-butyl-phenyl)-phenyleneamine ((dppy)BTPA); *N*,*N*′-di[(*N*-(3,6-di*tert*-butyl-carbazyl))-*n*-decyl] quinacridone (DtCDQA); *N*,*N*′-bis(1-naphyl)-*N*,*N*′-diphenyl-1,1′-biphenyl-4,4′-diamine (NPB)) are deposited through vapor deposition onto SiO_2 substrates that are prestructured with parallel gold stripes of various width. In such vapor deposition experiments, the ongoing processes often resemble epitaxial growth of inorganic materials: the molecules diffuse on the substrate, nucleate at favorable sites, and form growing islands. The prepatterning allows for a control of the nucleation and growth.[18]

Although the deposition and redistribution stages often occur successively, deposition may also still continue when the material is already being redistributed via diffusion or convective motion. Note that in particular for highly mobile deposit material, the distinction between the two transport processes, diffusion and convection, is not sharp when one deals with deposit amounts that allow at least locally for multilayer structures. Then one is already able to define a velocity profile within the film. In consequence, depending on the particular material properties and annealing parameters, one may expect that, depending on the location on the substrate, transport is dominated by diffusion in a surface layer of the deposit (as for solid films discussed, e.g., in refs 41 and 42), by diffusion of the bulk layer (as in dynamical density functional theory for diffusion of an adsorbate layer[43]), by convection with strong slip at the substrate (as for polymeric layers[44]), or by convection without slip (as for the majority of liquid layers[16,45]). In the long-wave models for the time evolution for surface profiles of the deposition layers or, more generally, for the adsorption at the substrate, these different transport mechanisms are related to power-law mobilities of different powers (zero, one, two, and three, respectively). A central aim of the present work is to clarify in which way a distinction of redistribution via the different transport mechanisms is important for the observed phenomena.

This is an important question as, e.g., in refs 17, 18 it is discussed that one of the employed molecules, DtCDQA, shows a liquid-like behavior while the other molecules (as e.g. NPB) behaves like a solid. In the latter, solid case, the height of the rather flat deposits always decreases with their width. In contrast, in the former (liquid) case, with increasing amounts of deposited molecules the DtCDQA assembles into droplets, elongated drops, molecule stripes, cylindrical ridges and ridges with bulges.[17] The height of the ridges increases with their width, an effect attributed to capillarity (constant contact angles).[18] Examples of structures obtained in these experiments are reproduced in Figures 1 and 2.

Note that the description as 'liquid-like behavior' in ref 46 is mainly based on the observed shape of the deposits (ridges with bulges) but not on an actual observation of the transport process or velocity profile across the deposit layer. Therefore, one might prefer to describe the behavior as dominated by interfacial tensions, i.e., capillarity. Other capillarity-dominated morphologies are obtained for DtCDQA on substrates with other patterns, e.g., with a cross-bar structure. Aspects of these experiments have already been described via kinetic Monte Carlo simulations on a lattice,[47] in particular, the transitions between growth that is localized on the gold stripes, the development of bulges that partly cover the bare substrate, and island formation everywhere on the susbtrate, which occur in dependence of the various interaction parameters.

Transformations between liquid ridges with and without bulges are also observed in macroscopic experiments with water.[39] There, bulges form when the contact angle for contact lines pinned at the step in wettability exceeds 90°. In the experiments with DtCDQA on Au-striped SiO_2, typical drop and ridge heights are often about 300 nm or below, and the equilibrium contact angles are below 22° (see ref 17). This implies that an important part of the profiles is at heights below

DOI: 10.1021/acs.langmuir.5b02407
Langmuir 2015, 31, 10618−10631

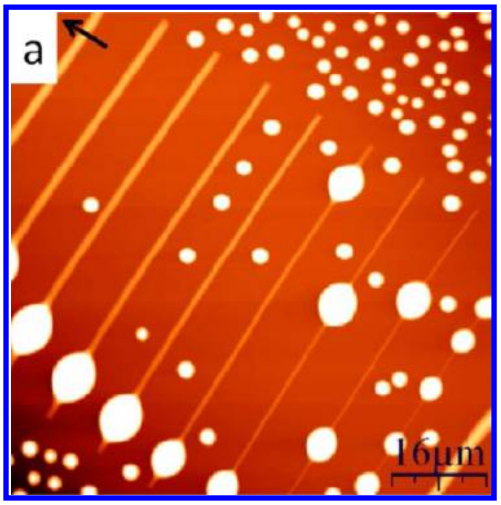

Figure 1. AFM image of DtCDQA molecules deposited on a SiO_2 substrate patterned with Au stripes. The width of the Au stripes increases from right to left from 0.3 to 2.3 μm. The mean film thickness is 50 nm. Since the diameter of one molecule is about 1 nm, this corresponds to roughly 50 monolayers. Reprinted with permission from ref 18. Copyright 2015 American Chemical Society.

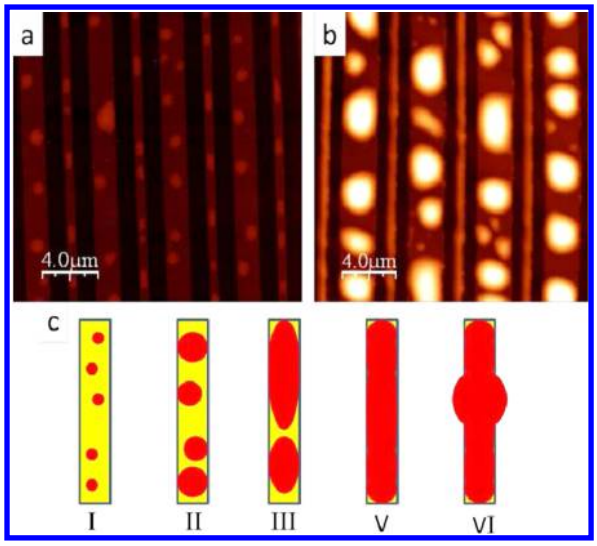

Figure 2. Different growth regimes during the deposition of DtCDQA molecules on SiO_2 substrates patterned with Au stripes of alternating width. Panels a and b show AFM images of 3 and 10 nm DtCDQA, respectively. Panel c shows sketches of the different growth regimes. For small amounts of deposited molecules, small droplets form on the Au lines (I). With increasing amount, larger droplets result until droplet edges reach the borders of the stripe (II), which become elongated (III). Finally, the whole stripe is covered with a cylindrical ridge (V). At a certain amount of molecules, bulges form that also cover part of the SiO_2 substrate. Picture reproduced from the Supporting Information section of ref 17. Copyright (c) 2015 WILEY-VCH Verlag GmbH & Co. KGaA.

100 nm. That is, the macroscopic theory does not directly apply to the experimental findings, and a disjoining pressure/wetting potential[48,49] should be incorporated in the description.

Here, we employ a mesoscopic continuum description to describe the deposition experiments. In particular, we are interested in the stability of transversally invariant ridges of material located on the more wettable gold stripes and, in general, the role of such ridge states in the course of the time evolution from a homogeneous deposited film of molecules toward a final bulge or drop geometry. We also consider the question of how the dominant redistribution mechanism (diffusion or convection) influences the evolution pathway. As our interest is in the static states *and* in the dynamic behavior, and because contact angles are small, we employ a gradient dynamics in small-slope approximation (i.e., a thin film or long-wave model),[16,45,50] which describes the temporal evolution of the film height profile of a thin layer of material as driven by wettability and capillarity. The heterogeneity of the substrate is modeled as a chemical heterogeneity that only affects the wettability similar to refs 24, 28, 30, and 32, where a number of different wetting energies (and therefore Derjaguin pressures) are used.

The focus of the analysis presented here lies on the different instabilities of a liquid ridge that result either in the formation of large bulges that spill from the more wettable stripes onto the less wettable bare substrate or in the formation of small droplets on the more wettable stripes. We perform a linear stability analysis of steady ridges using continuation techniques[51,52] as outlined in ref 24 and presented in tutorial form in ref 53. In particular, we analyze the influence of the wettability contrast, the amount of deposited material (mean film thickness), and the geometry of the stripe pattern on the stability of liquid ridges. Particular attention is given to an analysis of the influence of the main transport mechanism in the redistribution stage.

Our analysis allows us to identify and characterize the different growth regimes that are experimentally observed in ref 17 (here reproduced in Figure 2). Besides the instability where the ridge develops bulges that partly cover the less wettable substrate region, we describe a second transversal instability that lets very small ridges decay into droplets entirely on the more wettable stripe and show that it is related to the spinodal dewetting of a thin film on homogeneous substrates. The results of the stability analysis are supported by fully nonlinear time simulations.

The outline of the article is as follows. In Section 2 we introduce the gradient dynamics model for the case of a substrate with a wettability pattern. Next, we explain and illustrate in Section 3.1 the transversal linear stability analysis procedure employing a sinusoidal wettability pattern as example. Our results for a smoothed step-like wettability modulation are given in Section 3.2, while the cases of convective and diffusive transport are compared in Section 3.3. In the subsequent Section 4 we discuss numerical time simulations for the two different instabilities again considering various different transport mechanisms. We conclude and give an outlook in Section 5.

2. THE MODEL

We employ a mesoscopic continuum model to describe the dynamics of the redistribution process under the assumption that the slope of the free surface is small everywhere (long-wave or small gradient approximation[16,54]). In the case of purely convective dynamics, this assumption allows one to derive an asymptotic model from the governing equations of hydrodynamics that describes the time evolution of the height profile of a liquid film.[16,45,50] It reads

$$\partial_t h(\mathbf{x}, t) = \nabla\cdot\{Q(h)\nabla[P(h, \mathbf{x})]\} \quad (1)$$

DOI: 10.1021/acs.langmuir.5b02407
Langmuir 2015, 31, 10618−10631

with $\mathbf{x} = (x, y)^T$ and $\nabla = \left(\frac{\partial}{\partial x}, \frac{\partial}{\partial y}\right)^T$. Here, $Q(h) = h^3/(3\eta)$ is the mobility coefficient for a fluid where η is the dynamic viscosity. The generalized pressure $P(h, \mathbf{x})$ is given by

$$P(h, \mathbf{x}) = -\gamma\Delta h - \Pi(h, \mathbf{x}) \tag{2}$$

where γ is the liquid−gas surface tension in the Laplace pressure term and $\Pi(h, \mathbf{x})$ is the Derjaguin or disjoining pressure.[48,49,55] For the latter we use[56]

$$\Pi(h, \mathbf{x}) = \left(\frac{B}{h^6} - \frac{A}{h^3}\right)(1 + \rho g(\mathbf{x})) \tag{3}$$

Here the space-dependent term $\rho g(\mathbf{x})$ takes into account the chemical stripe pattern on the substrate. The dimensionless parameter ρ corresponds to the strength of the wettability contrast, whereas the function $g(\mathbf{x})$ is periodic and describes the geometry of the stripe pattern. From now on, we use nondimensional variables $\tilde{h}$, $\tilde{x}$, $\tilde{y}$, $\tilde{t}$ in such a way that the nondimensonal parameters 3 $\tilde{\eta}$, $\tilde{\gamma}$, $\tilde{A}$, $\tilde{B}$ are all equal to 1.[57] The tilde is then dropped in the following. The nondimensional precursor film height is then uniformly $h_p = 1$. Multiplying the term $1 + \rho\, g(\mathbf{x})$ to the disjoining pressure keeps h_p constant and only modulates the equilibrium contact angle as $\theta_0 = \sqrt{\frac{3}{5}(1 + \rho g(\mathbf{x}))}$. If the argument of the square root is negative, the liquid wets the substrate and $\theta_0 = 0$. Note that θ_0 is the angle in long-wave scaling, i.e., a small physical equilibrium contact angle $\theta_e = \epsilon\theta_0$ corresponds to a long-wave contact angle θ_0 of $O(1)$.

Finally, we note that the hydrodynamic thin film equation corresponds to a gradient dynamics of the underlying free energy (or interface Hamiltonian[58]). The pressure is given by the variation $P = \frac{\delta F}{\delta h}$ of the free energy $F = \int d\mathbf{x}\left[\frac{\gamma}{2}|\nabla h|^2 + f(h, \mathbf{x})\right]$, where the first term represents capillarity (interfacial energy of free surface) and the second term represents position-dependent wettability (wetting or adhesion energy or binding potential), which is connected to the disjoining pressure by $\Pi(h, \mathbf{x}) = -\partial_h f(h, \mathbf{x})$.[45,59] Note that the interpretation of the thin film equation (eq 1) as a gradient dynamics on the free energy functional allows one to go beyond the case of convective transport where the mobility is $Q(h) = h^3/(3\eta)$ in the case without slip at the substrate and $Q(h) = h^2/(3\eta)$ in the case with strong slip at the substrate.[44]

Indeed, by interpreting very small h rather as an adsorption normalized by a constant liquid bulk density than a film height, eq 1 becomes a general kinetic equation for the transport of material as driven by interfacial energies. Then, the term $\gamma\Delta h$ results from an energy density of diffuse interfaces between regions with low and with high adsorption, similar to the interfacial energy in a Cahn−Hilliard description of the decomposition of a binary mixture.[60] As the interfacial energies in both interpretations are determined by the same intermolecular interactions we do not expect a strong change in the value of the parameter γ, however, such changes may occur and can also be discussed.[61] In consequence, this extended interpretation allows one to investigate (i) transport via diffusion of the entire adsorbed film (then one uses the diffusive mobility $Q(h) \propto h$ as in dynamical density functional theory[43,62]), and as well (ii) transport via diffusion of a surface layer on the deposit as in typical solid-on-solid models (then one has a constant mobility $Q(h) \propto 1$[41,42]). Note that similar mobilities have been introduced in a piece-wise thin-film model for the formation and motion of droplets on composite (meltable) substrates.[63] In other contexts, similar equations with other mobilities occur, e.g., in a macroscopic phase-field model of unsaturated flow in porous media.[64] A comparative discussion and interpretation of result obtained with the various mobilities is provided below.

3. LINEAR STABILITY OF RIDGE STATES

3.1. Sinusoidal Wettability Pattern. To illustrate how a continuation method can be employed in the linear stability analysis, we first use a simple harmonic function of one independent variable x as a wettability pattern

$$g(\mathbf{x}) = \sin\left(\frac{2\pi x}{L_{\text{per}}}\right) \tag{4}$$

i.e., the substrate pattern is invariant in the y-direction. The domain size L is chosen equal to the period of the stripe pattern L_{per}. First, we determine steady solutions $h_0(x)$ of the one-dimensional system. Setting $\partial_t h = 0$ in eq 1 and integrating twice leads to

$$\partial_x^2 h_0(x) + \Pi(h_0, x) + C = 0 \tag{5}$$

The first integration constant corresponds to a net flux into or out of the integration domain and therefore vanishes in the case of horizontal substrates without additional lateral driving forces. The second integration constant C is the constant pressure inside the film that characterizes mechanical equilibrium. In the following, the constant pressure C is used as a continuation parameter that plays the role of a Lagrange multiplier, which ensures a constant deposit volume (as the density is assumed to be constant, here this is equivalent to mass conservation).

Such a one-dimensional solution can be extended homogeneously in the y-direction, thereby creating a steady solution of the two-dimensional thin film eq 1 that is translationally invariant in the y-direction, i.e., all y derivatives vanish. To determine the stability of such a solution, we allow for perturbations that depend in an arbitrary manner on x and are harmonic in the y direction. We use the ansatz

$$h(x, y, t) = h_0(x) + \epsilon h_1(x)\exp(\beta t + iqy) \tag{6}$$

where β is the growth rate, q is the transversal wavenumber, and $\epsilon \ll 1$. Introducing this ansatz into eq 1 leads to lowest order in ϵ to the linear eigenvalue equation

$$\begin{aligned}\beta h_1 = &-Q(h_0)(\partial_x^2 - q^2)[(\partial_x^2 - q^2)h_1 + (\partial_h\Pi(h_0, x))h_1] \\ &- (\partial_x Q(h_0))\partial_x[(\partial_x^2 - q^2)h_1 + (\partial_h\Pi(h_0, x))h_1]\end{aligned} \tag{7}$$

that has to be solved for unknown β and $h_1(x)$. We solve the time-independent eq 5 and the eigenvalue problem 7 in parallel using pseudoarclength continuation as implemented in the continuation toolbox AUTO-07p.[65,66] The specific set of equations treated by AUTO-07p is given in the Supporting Information. Tutorials are provided in ref 67 (see in particular tutorials `drop`, `hetdrop`, and `lindrop`).

The desired results are obtained through a number of continuation runs: We start with the trivial solution $h_0(x) = \bar{h} =$ const. and $h_1 = 0$, set $\rho,\beta = 0$, and $C = -\Pi(\bar{h},x)$, whereas the parameter q is fixed at some small positive value. We continue this solution as we change the wettability contrast ρ. This yields the solution branches that form the bifurcation diagram presented in Figure 3a,b in terms of the norm and energy of

DOI: 10.1021/acs.langmuir.5b02407
Langmuir 2015, 31, 10618−10631

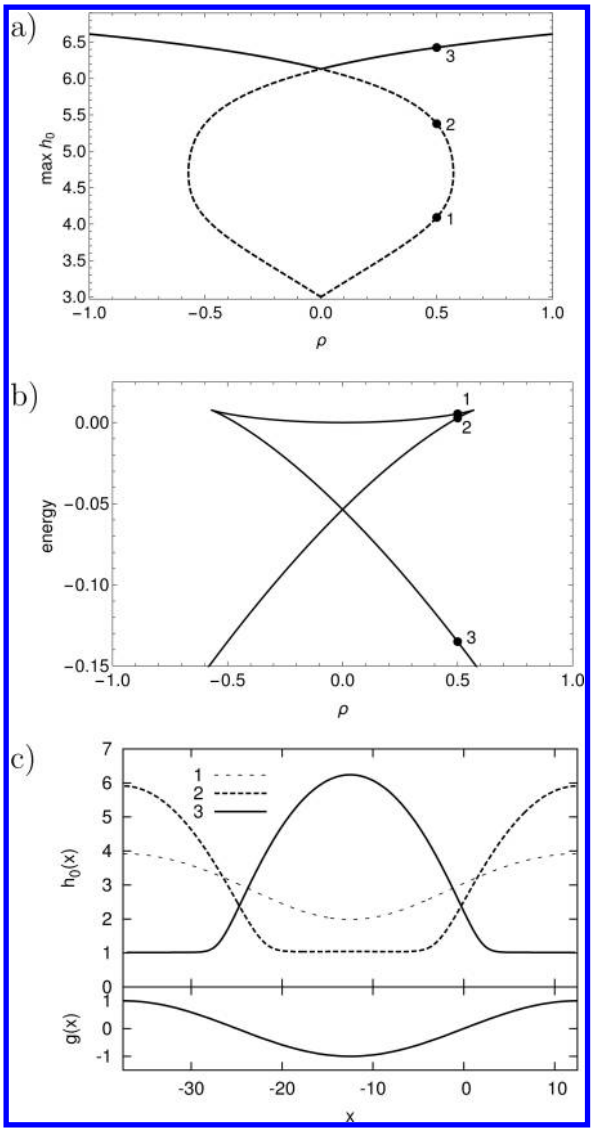

Figure 3. Panels a and b give bifurcation diagrams in terms of the maximal film height and energy, respectively, as a function of wettability contrast ρ at $\bar{h} = 3$ and $L_{per} = 50$. The solution branches are obtained from eqs 5 and 7 using pseudoarclength continuation. The solid and dashed parts of the branches in panel a represent stable and unstable solutions, respectively. The top part of panel c gives solution profiles 1, 2, and 3 corresponding to loci indicated by bullet symbols in panels a and b. Solutions 1 and 2 are unstable and have more liquid on the low wettability stripe. Solution 3 is the one of lowest energy, and represents a stable drop on the more wettable patch. The bottom part of panel c gives the inhomogeneity profile $g(x)$ (cf. eq 4). The more (less) wettable area corresponds to $g(x) \approx -1$ ($g(x) \approx 1$).

the solutions, respectively. Figure 3c provides three corresponding examples of ridge/trench cross sections according to the labels in panels a and b.

In the next step, we start at a specific point on the stable part of the solution branch for positive ρ and let the growth rate β vary. As h_1 is initially zero, and h_0 is independent of β, the solution does not change with β. However, when β crosses a value of the discrete eigenspectrum, a branching point is detected as a solution branch with $h_1 \neq 0$ bifurcates vertically, i.e., because of the linear character of the eigenvalue problem, the entire emerging branch that consists of eigenfunctions with all possible amplitudes is located at the same single value of the control parameter β. A tutorial for this technique is available.[53]

In the next run, one follows this new branch, effectively only changing the amplitude of h_1 at fixed β. The norm $\|h_1\| = \left(\frac{1}{L}\int_0^L h_1^2\,dx\right)^{1/2}$ is introduced as an additional continuation parameter via an integral condition, and the run is stopped when $\|h_1\| = 1$. This value is kept in all subsequent continuation steps.

Figure 4a shows the first two eigenmodes of eq 7. The symmetric eigenmode (solid line) corresponds to a so-called

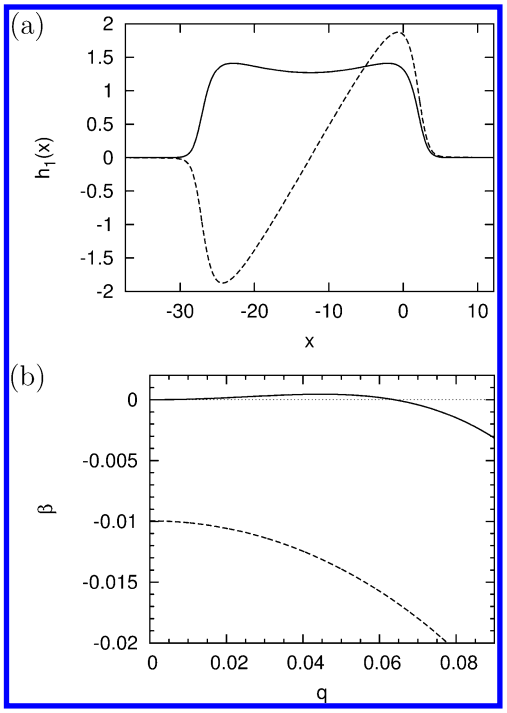

Figure 4. (a) The two most important eigenmodes of eq 7. The solid curve is an unstable varicose mode; the dashed curve is a stable zigzag mode ($\rho = 0.5$, $\bar{h} = 3$). (b) Dispersion relations of the two critical modes shown in panel a. The varicose mode (solid line) has a band of finite wavelengths with positive growth rates. Therefore, the analyzed ridge is linearly unstable with regard to this mode, whereas the zigzag mode (dashed) is always stable for the system in question.

varicose mode and is unstable, whereas the antisymmetric zigzag eigenmode (dashed line) is stable.[24,68] In the unstable q-range, the ridge is linearly unstable with regard to an instability often called a Rayleigh−Plateau instability (cf. refs 24 and 28 for related thin film systems).

Now one fixes the norm $\|h_1\| = 1$ and continues the eigenvalue problem in the parameters β and q to directly compute the dispersion relation $\beta(q)$ for each eigenmode. The results for both varicose and zigzag modes are shown in Figure 4b. The varicose mode has a finite band of unstable wavenumbers $0 < q < q_c$ similar to the case of a homogeneous substrate. The growth rate at $q = 0$ is always zero for the varicose mode: $\beta(q = 0) = 0$ corresponding to mass conservation. The zigzag mode is always stable for the present system. On a homogeneous substrate $\beta(q = 0) = 0$ reflects the translational invariance in the x direction.[24] In contrast, here this invariance is broken by the stripe wettability pattern implying that $\beta(q = 0) \neq 0$. Note that the zigzag mode might

DOI: 10.1021/acs.langmuir.5b02407
Langmuir 2015, 31, 10618−10631

become unstable under driving in the x direction, e.g., on an incline.[69]

Now we consider the dispersion relation $\beta(q)$ and write it as $q(\beta)$. Then the maximum of $\beta(q)$ becomes a fold of the curve $q(\beta)$, i.e., with β as the primary bifurcation parameter, it appears as saddle-node bifurcation. With this trick, one is able to detect the maximum of $\beta(q)$ when continuing the eigenvalue problem in the parameters β and q. Then the fold continuation modus of AUTO-07p is employed to follow the maximum of the dispersion relation when varying some other parameter. Here, we follow the maximum β_{max} of $\beta(q)$ for the varicose mode varying, e.g., $\overline{h}$, until β_{max} is extremely small, i.e., $\beta_{max} \approx 0$. Fixing this β_{max} at the particular small value, we then track the instability threshold as a final fold continuation in the plane spanned by $\overline{h}$ and ρ. This allows us to obtain the stability diagram for ridges presented in Figure 5.

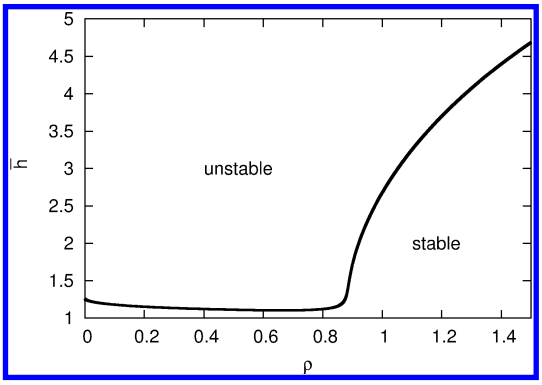

Figure 5. Linear stability diagram in the $[\rho, \overline{h}]$ plane. The solid line shows the linear stability threshold for a homogeneous ridge solution. For parameters below and above the curve, ridges are linearly stable and unstable, respectively.

For large wettability contrasts ρ, the stability threshold with respect to $\overline{h}$ increases monotonically with ρ. This is the behavior we expect from the experimental findings. For small ρ, however, this is no longer true. We will discuss this surprising result at the end of the next section.

3.2. Smoothed-Step Stripe-Like Inhomogeneities. In the previous section we have introduced our methodology using a simple sinusoidal wettability modulation. Now we use a spatial modulation of the disjoining pressure that realistically reflects the experimentally employed chemical stripe pattern. We use smoothed steps using for a single period

$$g(x) = \tanh\left[\frac{1}{l_s}\left(x_A - \left(\frac{x}{L_{per}}\right)\right)\right] \times \tanh\left[\frac{1}{l_s}\left((1 - x_A) - \left(\frac{x}{L_{per}}\right)\right)\right] \quad (8)$$

Figure 7c shows an example of the function $g(x)$. The parameter L_{per} is the spatial period as before, $l_s L_{per}$ is the width of the transition region between the more wettable stripe (MWS) and the less wettable stripe (LWS). That is, l_s defines the sharpness of the wettability contrast. The MWS ($g(x) \approx -1$) starts at $x_A L_{per}$ and ends at $(1 - x_A) L_{per}$ in each period. The smaller x_A is, the wider the MWS.

We start with a domain size equal to the period of the stripe pattern $L_{per} = 50$ and set $x_A = 0.3$ so that the MWS is thinner than the LWS. The parameter l_s is set to 0.03. As in the previous section, the starting solution is the trivial one $h_0 = \overline{h} = 3$. We continue this solution as ρ is varied and obtain the solution branch shown in Figure 6. Since the MWS is thinner than the LWS, the symmetry between positive and negative ρ,

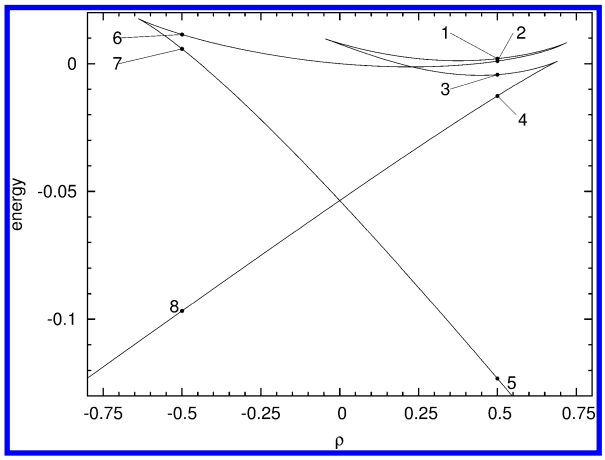

Figure 6. Solution branches obtained by a first continuation in the wettability contrast ρ. As in Figure 3, we use the energy as a solution measure in order to assess the stability of the solutions: Only solutions of lowest energy are stable, i.e., solution branches where solutions 5 and 8 are situated. The solutions corresponding to the labels 1−8 are shown in Figure 7. The parameters are $L_{per} = 50$, $l_s = 0.03$, $\overline{h} = 3$ and $x_A = 0.3$.

which could be seen in Figure 3a for sinusoidal wettability patterns, is broken. Figure 7 shows different stable and unstable solutions for $\rho = 0.5$ (Figure 7a) and $\rho = -0.5$ (Figure 7b), respectively. For positive ρ we find a larger variety of unstable solutions, e.g., configurations with a small drop on the MWS and a larger drop on the LWS. Notice that solution five, the one with the lowest energy, is the only stable solution for positive ρ.

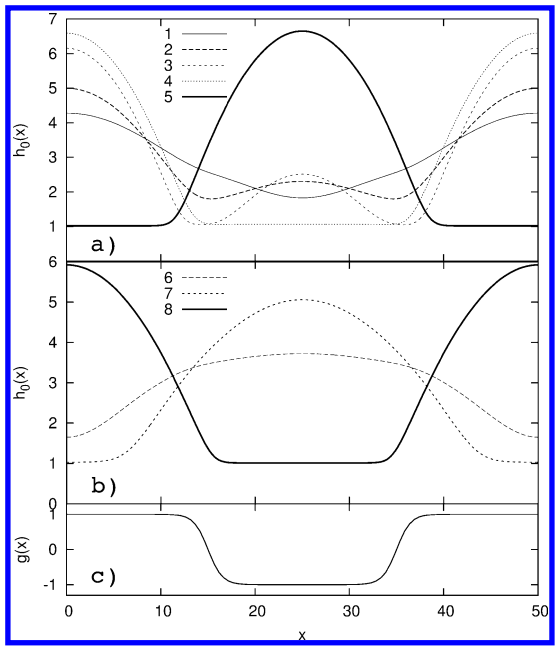

Figure 7. Steady solutions corresponding to the labels (a) 1−5 and (b) 6−8 of Figure 6 for $\rho = 0.5$ ($\rho = -0.5$), $L_{per} = 50$, $l_s = 0.03$, $\overline{h} = 3$, and $x_A = 0.3$. As ρ is positive (negative), the more wettable area corresponds to the region where $g(x) \approx -1$ ($g(x) \approx 1$). Here, solutions five (a) and eight (b) are the only stable solutions. (c) The inhomogeneity function $g(x)$, given by eq 8.

DOI: 10.1021/acs.langmuir.5b02407
Langmuir 2015, 31, 10618−10631

For negative values of ρ, solution eight is the only stable solution.

From now on, we focus on the experimentally studied (see ref 17) case of narrow stripes of more wettable material and restrict ourselves to the case of positive ρ. As in the previous section, we directly compute the linear stability diagram on the $[\rho, \bar{h}]$ plane. The result is shown as the solid line in Figure 8. In

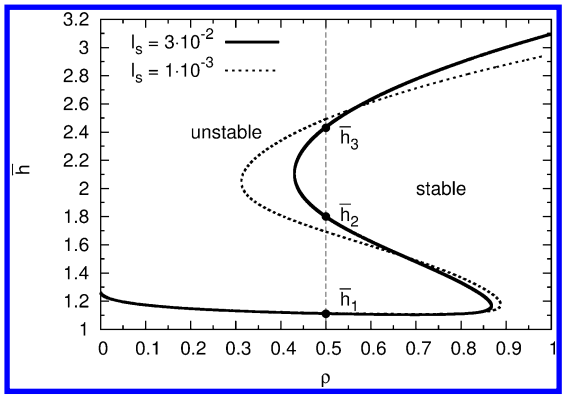

Figure 8. Linear stability diagram in the $[\rho, \bar{h}]$ plane for steep wettability gradients between the stripes. In particular, $l_s = 0.03$ (solid line) and $l_s = 0.001$ (dotted line). For $\rho = 0.5$ there are three stability thresholds $\bar{h}_1$, $\bar{h}_2$, and $\bar{h}_3$.

contrast to the example with the sinusoidal wettability modulation (Figure 5), the curve has an essentially non-monotonous form. In the region $0.43 \lesssim \rho \lesssim 0.87$, there are four different stability regions that deserve further investigation. To this end, we consider the system for a constant $\rho = 0.5$.

For $\rho = 0.5$ we observe three critical values of the mean film thickness $\bar{h}$, $\bar{h}_1 \approx 1.1$, $\bar{h}_2 \approx 1.8$, and $\bar{h}_3 \approx 2.4$. We continue the stable one-dimensional solution $h_0(x)$ and its critical eigenfunction $h_1(x)$ in the mean film thickness $\bar{h}$. Figure 9 shows the obtained profiles $h_0(x)$ and eigenmodes $h_1(x)$, respectively. In Figure 10a, we give the maximal growth rates

$$\beta_{\max} = \max_q \beta(q) = \beta(q_{\max}) \tag{9}$$

and the corresponding $q_{\max}$ in the unstable regions $\bar{h}_1 < \bar{h} < \bar{h}_2$ and $\bar{h} > \bar{h}_3$. In the stable regions $\bar{h} < \bar{h}_1$ and $\bar{h}_2 < \bar{h} < \bar{h}_3$, $\beta_{\max} = q_{\max} = 0$.

For very thin films ($\bar{h} < \bar{h}_1$), the one-dimensional solutions are not yet droplets. They are better described as piecewise flat films with a higher mean film thickness on the MWS (cf. solution for $\bar{h} = 1.05$ in Figure 9a) with an eigenmode corresponding to the slowest relaxing mode that reflects a modulation of this film height everywhere in the system (Figure 9b for $\bar{h} = 1.05$). The flat film pieces are sufficiently thin to be below the instability threshold for spinodal dewetting on respective homogeneous substrates. Therefore, the piecewise flat film solutions are stable, also in two dimensions. For $\bar{h}_1 < \bar{h} < \bar{h}_2$, the one-dimensional solutions have a pronounced droplet shape (cf. solution for $\bar{h} = 1.5$ in Figure 9a). The corresponding two-dimensional ridge solutions are not stable, the shape of the critical eigenfunction $h_1(x)$ is depicted in Figure 9 (b) for different $\bar{h}$. The profile of $h_1(x)$ has only one maximum and corresponds to an instability mode that varies the height of the ridge, but does nearly not move the contact line region (cf. the top panel of Figure 11, where we show $h_0 \pm \delta h_1$, with δ being a small constant). As we will see below, in the nonlinear regime, this mode results in the decay of the ridge into droplets *on* the

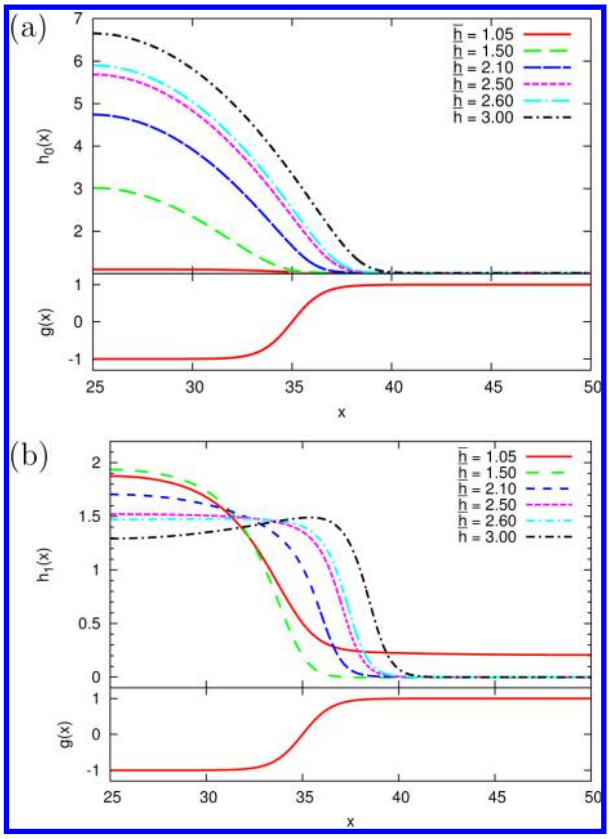

Figure 9. Top panels: Stationary solutions $h_0(x)$ (a) and critical eigenfunction $h_1(x)$ (b) for $\rho = 0.5$ and different mean film heights $\bar{h}$. At $2.5 < \bar{h} < 2.6$, the transition between a unimodal and a bimodal shape occurs. Bottom panels: The inhomogeneity function $g(x)$, given by eq 8.

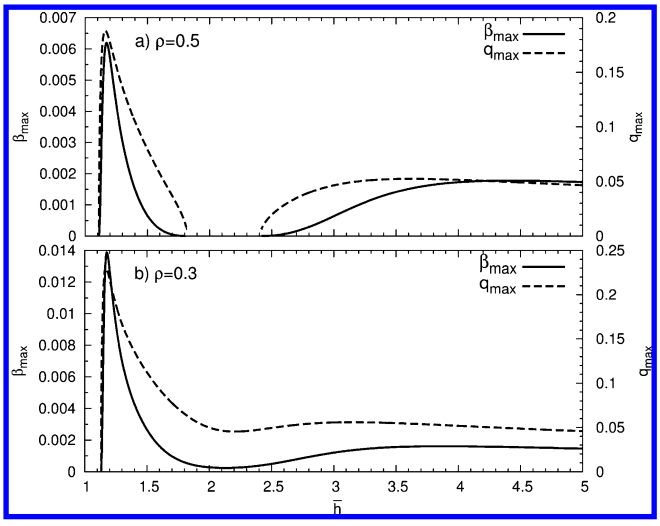

Figure 10. Maximal growth rates $\beta_{\max}$ and the corresponding $q_{\max}$, which are defined in eq 9, against $\bar{h}$ for (a) $\rho = 0.5$ and (b) $\rho = 0.3$.

MWS and therefore belongs to the growth regimes I to III observed in the experiments, which are sketched in Figure 2.

In the region $\bar{h}_2 < \bar{h} < \bar{h}_3$, the critical eigenfunction still has only one maximum, but the growth rates are negative for finite wavenumbers (and zero for $q = 0$). In this region, a ridge on the MWS is stable because it is no longer possible for the ridge to form droplets *on* the MWS. This can be seen from the critical eigenfunction at $\bar{h} = 2.1$ in Figure 9b. It becomes broader than

DOI: 10.1021/acs.langmuir.5b02407
Langmuir 2015, 31, 10618−10631

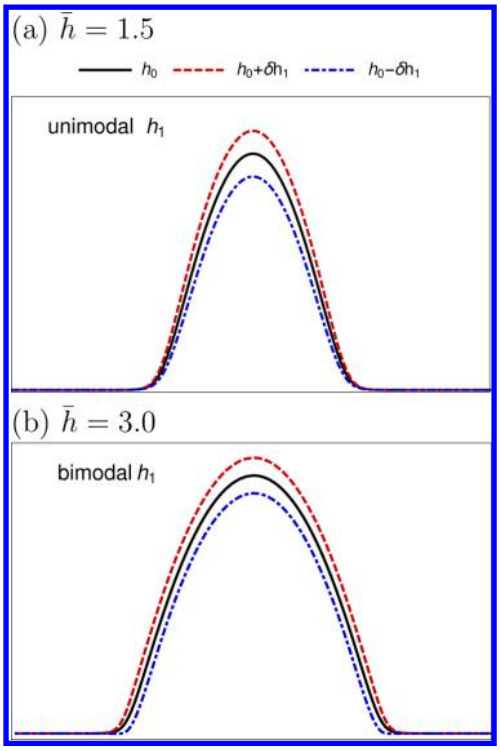

Figure 11. Comparison of transversal instabilities with a unimodal eigenfunction $h_1(x)$ for small film heights (panel a, $\bar{h}$ = 1.5) and a bimodal $h_1(x)$ for larger film heights (panel b, $\bar{h}$ = 3.0). Shown are the steady ridge profiles (solid black curves) together with the sum and difference of the ridge profile and the eigenfunction multiplied by a small constant δ (red dashed and blue dot-dashed curves, respectively). In the first case, the contact line stays fixed; in the second case it is shifted.

the MWS. Since in this region it is not yet energetically favorable for the ridge to leave the stripe, the ridge stabilizes. This corresponds to the growth regime V seen in the experiments.

For mean film heights above $\bar{h}_3$, it becomes energetically favorable for the liquid to also cover part of the LWS, and the maximal growth rate becomes positive (cf. Figure 10a). At a critical film thickness of $\bar{h}^* \approx 2.5$, slightly greater than $\bar{h}_3 \approx 2.4$, the critical eigenfunction undergoes a shape transition from unimodal to bimodal. The eigenfunction has two symmetric maxima corresponding to the narrowing/broadening of the ridge so that the contact line shifts if one adds [subtracts] $h_1(x)$ to [from] the steady ridge solution (cf. the bottom panel of Figure 11). It is shown below that this mode results in the nonlinear regime in the formation of bulges that partly cover the LWS, indicating that the region $\bar{h} > \bar{h}_3$ corresponds to the growth regime VI observed in experiment (cf. Figure 2).

For small wettability contrasts ($\rho \lesssim 0.43$) we observe the same shape transition in the critical eigenmode, but the maximal growth rate remains positive for $\bar{h}$ above the curve in Figure 8. This is demonstrated in Figure 11b for ρ = 0.3.

As a next step we take a look at the influence of the sharpness of the wettability transition. The dotted line in Figure 8 shows the stability threshold in the $[\rho, \bar{h}]$ plane for l_s = 0.001, i.e. for a sharper wettability transition. In this case, stable ridges are possible for lower wettability contrasts ρ. On the other hand, for $\rho \gtrsim 0.57$, the onset of the Rayleigh-Plateau instability is shifted toward lower $\bar{h}$. This is probably due to the fact that the effective width of the MWS decreases with decreasing l_s. Further decreasing l_s does not lead to a significant change of the diagram, therefore l_s = 0.001 can already be seen as the limiting case of a true step function.

Finally, we remark that the instability threshold in Figure 8 reaches the value $\bar{h} \approx 1.26$ at ρ = 0, as is the case for the sinusoidal wettability modulation in Figure 5 above. This value of $\bar{h} \approx 1.26$ corresponds, as it should be, to the analytically obtained threshold of the spinodal instability of a flat film, which is given by $\partial\Pi/\partial h = 0$. This reinforces the interpretation that the first instability for small ρ and $\bar{h}$ is a spinodal dewetting instability. As one increases ρ from zero to a small finite values while keeping $\bar{h}$ constant, the one-dimensional flat film solutions change toward more and more pronounced droplet solutions with increasing maximal film heights. This explains why for small ρ the lower instability threshold in terms of $\bar{h}$ decreases with increasing ρ.

3.3. Comparison of Diffusive and Convective Transport. Equation 5, which determines the equilibrium morphologies, does not depend on the mobility term $Q(h)$ as long as it is nonzero, whereas in the eigenvalue eq 7, $Q(h_0)$ also enters. Hence, the mobility has an effect on the absolute values of β when $\beta \neq 0$, but does not influence the position of the instability thresholds β = 0 in parameter space. This is demonstrated in Figure 12, where we plot, as in Figure 10a, the

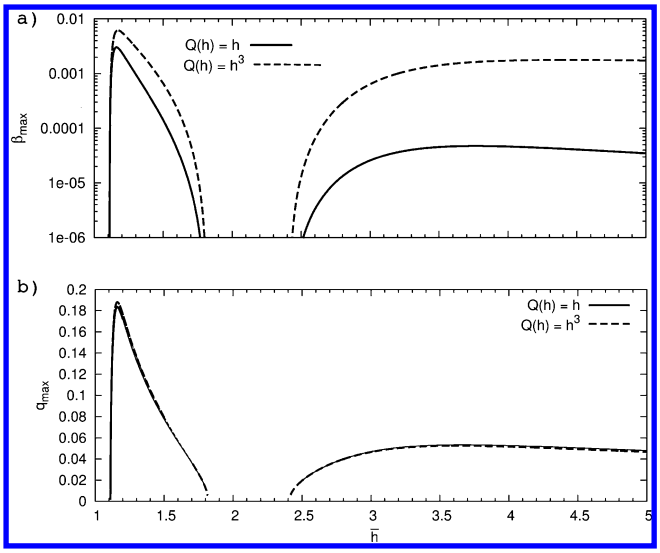

Figure 12. (a) Maximal growth rates of the transversal instability for ρ = 0.5 against $\bar{h}$. The dotted line corresponds to a convective mobility $Q(h) = h^3$. This curve is the same as in Figure 10a, but in logarithmic scaling. The solid line corresponds to a diffusive mobility term h. (b) The corresponding fastest growing wavenumbers. The growth rates are significantly larger for the convective instability, especially in the bulge formation regime. The fastest growing wavenumbers are almost identical for both mobilities.

maximum of the dispersion relation β_{max} against the mean film height $\bar{h}$ for convective and diffusive mobility functions $Q(h) \sim h^3$ and $Q(h) \sim h$, respectively (note the semilog scale in the upper panel). Although the absolute values are dramatically smaller for the diffusive mobility $Q(h) = h$, the stability thresholds β_{max} = 0 remain at the same position, as can be seen more clearly in the bottom panel, where the corresponding q_{max} is shown as a function of $\bar{h}$. Therefore, we argue that the specific mobility that results from the particular dominant transport process(es) influences neither the linear stability of the ridges nor the observed equilibrium morphologies. Only the

DOI: 10.1021/acs.langmuir.5b02407
Langmuir 2015, 31, 10618−10631

time scales at which the instabilities grow depend on the mobility. This point will be further elucidated in the subsequent section where we consider the time evolution in the fully nonlinear regime.

4. TIME SIMULATIONS

In the previous section we showed that a steady ridge solution becomes transversely unstable with regard to a varicose instability mode if one changes control parameters of the system. Furthermore, the eigenfunction $h_1(x)$ of the varicose mode continuously changes its shape with parameters. As a result, two different types of transversal instability (both varicose modes) can occur in different ranges of the parameters wettability contrast and amount of deposited material. In particular, at fixed wettability contrast, for small volume a mode results with a pinned triple line, and for a larger volume another one where the triple line is not pinned. Depending on the location in parameter space, the two instability regimes can be separated by a range of stable ridges. Note that it is normally not possible to deduce the final fully nonlinear morphology from the linear results. Therefore, we next investigate with fully nonlinear time simulations of eq 1 in the two parameter regimes whether the two instability modes coincide with two different nonlinear evolutions, i.e., with ridges decaying into droplets that only cover the MWS and ridges that evolve into bulges that also cover part of the LWS, respectively.

The numerical simulations are performed employing the alternating direction implicit (ADI) method. Thereby the spatial and time derivatives are discretized using second-order finite differences. This results in a nonlinear system of equations that is solved at each time step using Newton's method. In each Newton iteration a linear system (Jacobian matrix of the nonlinear system) is efficiently solved employing the ADI method (see refs 70 and 71 for more details).

The first simulation is performed at low volume, for $\bar{h} = 1.16$. This value is close to the first critical value of the mean film thickness $\bar{h}_1$ (cf. Figure 8), where the ridge becomes transversally unstable with regard to the unimodal varicose eigenmode, and we expect that droplets emerge that only cover the MWS. This value also corresponds to the maximum of β_{max} that coincides with the maximum of q_{max} (cf. Figure 11a), in order to minimize the necessary computation time and domain size. The latter is then selected as 50 in the x- and 100 in the y-direction.

In the course of the time evolution, we measure the non-dimensional free energy $F(t) = \int \mathrm{d}x\mathrm{d}y\left[\frac{1}{2}|\nabla h|^2 + f(h, x)\right]$, where $f(h, x)$ now stands for the nondimensional wetting potential. Note that the total time derivative of the free energy is given by $\frac{\mathrm{d}F}{\mathrm{d}t} = -\int Q(h)\left(\frac{\delta F}{\delta h}\right)^2 \mathrm{d}x\mathrm{d}y$. As the mobility function $Q(h)$ is always positive, the final expression is negative, i.e., F is a Lyapunov functional. As a consequence, linearly stable and unstable steady solutions of the thin film equation correspond to local minima or saddle points of the free energy functional F, respectively. The resulting dependency of energy on time is shown in Figure 13. In this energy time series obtained with the convective mobility function $Q(h)$ (dashed red curve), one can identify four plateaus of different length where the evolution approaches different steady states of the system. The first three correspond to unstable steady profiles, while the final one corresponds to the absolutely stable steady state configuration. All four configurations for $Q(h) = h^3$ are depicted in Figure 14.

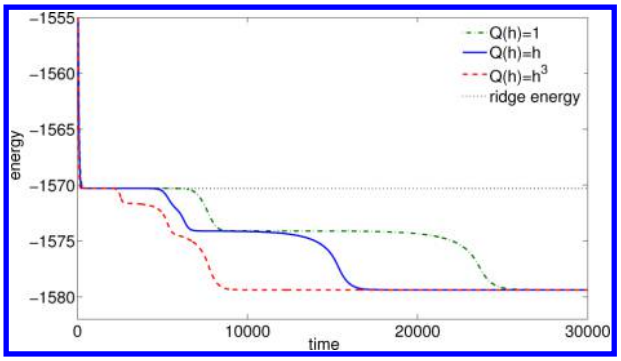

Figure 13. Time series of the energy during a direct numerical simulation of the thin film eq 1 with $\bar{h} = 1.16$ for transport by surface diffusion (mobility $Q(h) \sim 1$, dash-dotted green curve), by bulk diffusion ($Q(h) \sim h$, solid blue line), and by convection ($Q(h) \sim h^3$, dashed red line). The configurations that correspond to the four energy plateaus for $Q(h) = h^3$ are plotted in Figure 14.

The first configuration, which is assumed very quickly starting from a flat film perturbed by small-amplitude noise, is a transversally invariant ridge that is identical to the one obtained above through one-dimensional steady state continuation. In Figure 14a and Figure 15, the solutions resulting from the direct numerical simulation (dotted line) and of the one-dimensional continuation (solid line) are compared. The fact that this unstable steady state is assumed for a considerably long time during the time simulation retrospectively justifies the approach of the transversal linear stability analysis of the previous section. After a certain time, the homogeneous ridge develops transversal modulations that grow exponentially and evolve into the three droplet state that corresponds to the second plateau and is depicted in Figure 14b. Two of the drops shrink and vanish in subsequent coarsening events until only one droplet remains (Figure 14c,d). The borders between the LWS and MWS in Figure 14 are indicated by dashed black lines. From this one can see that the droplets are completely located on the MWS, in agreement with the experimental case (I) and with the discussion in the previous section.

To further characterize the departure of the time evolution from the ridge state of the first plateau, Figure 16 (solid line) shows the time evolution of the logarithm of the difference ΔF between the energy $F(t)$ and the reference energy F_0 of the ridge solution $h = h_0(\mathbf{x})$. One observes that for the time interval when the system is close to the unstable ridge solution (cf. Figure 14a,b), the energy ΔF grows exponentially with a growth rate $2\beta_{max}$ (dashed curve) as expected from the transversal linear stability analysis. Here, $\beta_{max} = \beta(q_{max})$ is the growth rate, calculated for the most unstable mode of the transversally invariant ridge solution. Indeed, an expansion of the energy $F(t)$ about the ridge solution h_0 with the perturbed solution of the form $h = h_0 + \varepsilon h_1(\mathbf{x})\exp(\beta t)$ reads

$$F(t) = F_0 + \varepsilon \int \mathrm{d}\mathbf{x} \left.\frac{\delta F}{\delta h}\right|_{h=h_0} h_1(\mathbf{x}) e^{\beta t} + \varepsilon^2 \int \mathrm{d}\mathbf{x} \left.\frac{\delta^2 F}{\delta h^2}\right|_{h=h_0} h_1(\mathbf{x})^2 e^{2\beta t} + \text{h.o.t}$$

As the linear part in ε of this expansion vanishes at $h = h_0$, the nontrivial term of lowest order is the quadratic one, explaining the growth rate of 2β.

DOI: 10.1021/acs.langmuir.5b02407
Langmuir 2015, 31, 10618−10631

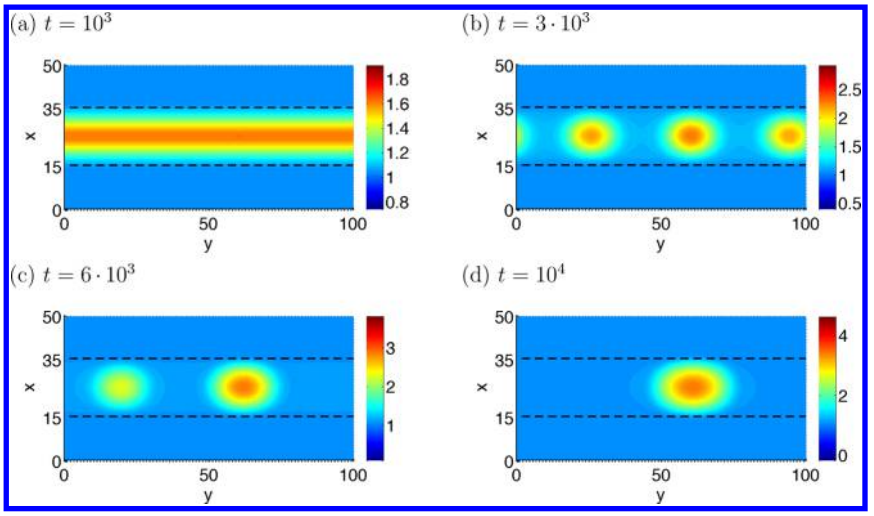

Figure 14. Snapshots of a direct time simulation of the thin film eq 1 with $\bar{h}$ = 1.16, l_s = 0.03, x_A = 0.3, L_{per} = 50 in the case of purely convective transport (mobility $Q(h) = h^3$). The borders of the MWS is indicated by dashed (black) lines. Figure 13 shows the corresponding time series of the energy $F(t)$. The four snapshots at times t = 1000, 3000, 6000, 10000 correspond to the four energy plateaus in Figure 13.

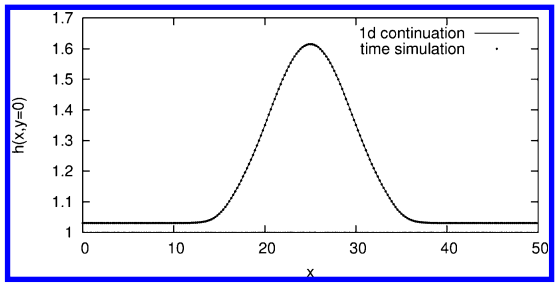

Figure 15. Comparison between solutions that result from the one-dimensional continuation (solid line) and from the direct time simulation (where the dotted line gives the profile of a cross-section at y = 0 and t = 1000 of the transversally invariant ridge state assumed for a long intervall in the time evolution, cf. Figure 14a.

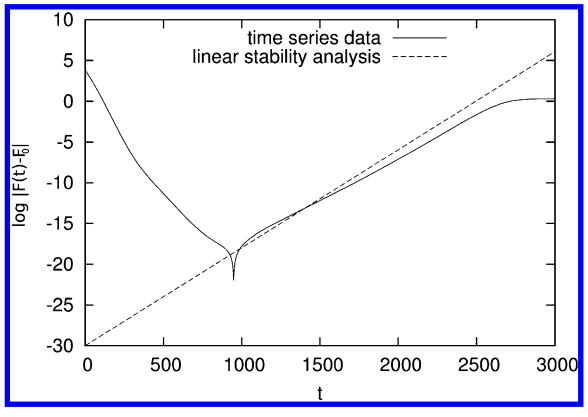

Figure 16. Solid line gives log $|F(t) - F_0|$, where F_0 is the free energy of the steady transversally invariant ridge state h_0, and $F(t)$ is the free energy at time t during the time simulation in Figure 14. The dashed curve shows the exponential growth with a growth rate of $2\beta_m$ that one expects from the linear stability analysis with regard to transversal modes.

Note that the transient behavior of the energy $F(t)$ changes when employing different mobility functions $Q(h)$. The solid blue and green dash-dotted lines in Figure 13 give the result for linear (bulk diffusion) and constant (surface diffusion) mobilities, respectively. Remarkably, one clearly sees that the same energy plateaus appear independent of the chosen mobility; however, their relative duration depends on the particular chosen transport behavior. For instance, with the convective mobility after the ridge configuration, the evolution visits the three drop solution that is still visible as a shoulder with the linear mobility and is only barely visible (when zooming in) with the constant mobility. The two-drop solution is clearly visited by all evolutions, and the final configuration (corresponding to the single drop solution) is the same for all mobilities $Q(h)$, which is expected as F is a Lyapunov functional, independent of the mobility.

Next, we analyze the time evolution at identical wettability contrast ρ = 0.5 but larger mean film height $\bar{h}$= 1.9 in the parameter range where, according to the linear stability analysis in the previous section, the ridge is unstable with respect to the second type of transversal instability, i.e., with respect to the bimodal varicose eigenmode, and we expect that ridges that evolve into bulges also cover part of the LWS. Figure 17 shows four snapshots from this time simulation for a convective mobility $Q(h) = h^3$, whereas Figure 18 gives the corresponding dependence of the energy on time for convective ($\sim h^3$, red dashed line) and surface diffusion ($\sim$1, solid blue line) mobilities $Q(h)$). In addition, Figure 19 shows a zoom into the energy evolution for the final thousand time steps (in logarithmic scale). There, the letters a–d correspond to the snapshots from the time simulations that correspond to the various plateaus. As in the previous case, the transversally invariant ridge is assumed quickly (Figure 17a) and forms the starting point for the subsequent morphological transitions. Note, however, that here the ridge solution is accompanied by a single small drop, situated on the LWS. The existence of the state with this drop results in a shoulder in the energy plot at about $t = 10^4$ (cf. Figure 19). After a short time, the drop shrinks and disappears, and the system stays close to the unstable steady transversally invariant ridge (with energy F_r) for some time (see the short energy plateau in Figure 19 for $Q(h) = h^3$ close to F_r). Eventually the ridge develops modulations in y-direction (see panel (b) of Figure 17). These modulations grow and form two large bulges (Figure 17c and Figure 19 at $F = F_d$). Finally, one of them vanishes in a coarsening event, and only one bulge remains (panel d of Figure 17 and Figure 19 at

DOI: 10.1021/acs.langmuir.5b02407
Langmuir 2015, 31, 10618–10631

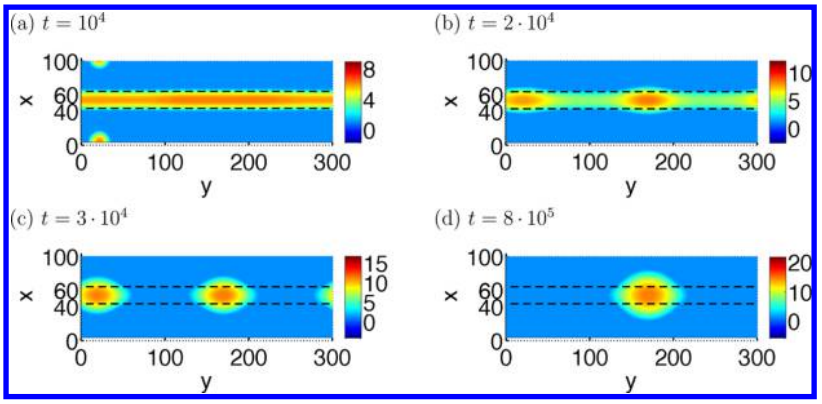

Figure 17. Snapshots of a direct time simulation of eq 1 at $\overline{h} = 1.9$, $\rho = 0.5$, $l_s = 0.015$, $x_A = 0.4$, and $L_{per} = 100$ and a convective mobility $Q(h) = h^3$. Panels a, b, c, and d show snapshots at times $t = 10^4$, $t = 2 \times 10^4$, $t = 3 \times 10^4$, and $t = 8 \times 10^5$, respectively. The borders of the more wettable stripes (MWS) are indicated by dashed (black) lines.

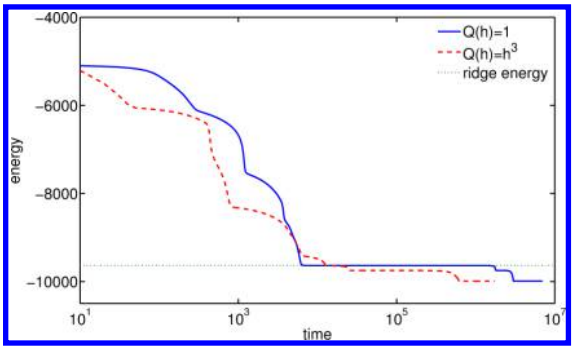

Figure 18. Time series of the free energy during the time simulation of eq 1 with $\overline{h} = 1.9$ for transport by surface diffusion (mobility $Q(h) \sim 1$, solid blue line) and by convection ($Q(h) \sim h^3$, dashed red line). The configurations that correspond to the last four energy plateaus for $Q(h) = h^3$ are given in Figure 17.

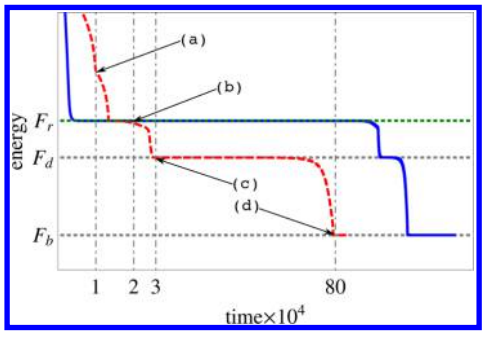

Figure 19. A zoom into the final thousand time steps in the energy plot (Figure 18) for the time simulation of eq 1 with $\overline{h} = 1.9$ for transport by surface diffusion (mobility $Q(h) \sim 1$, solid blue line) and by convection ($Q(h) \sim h^3$, dashed red line). The letters a–d refer to snapshots from DNS (cf. Figure 17) that correspond to the last four energy plateaus for $Q(h) = h^3$ (right).

$F = F_b$. From the dashed black line, indicating the borders of the wettability regime, one can see that in this case the solution is not pinned to the MWS and also covers the LWS. The emerged configurations resemble the experimentally observed case VI (see Figure 2). Notice that, in this case, bulges can possess long sleeves along the stripe or be isolated (cf. Figure 1). A study of the transition between both possible final configurations involves a detailed analysis of shape transitions, which is not within the scope of the current study.

However, for larger initial film heights $\overline{h}$, the seemingly final bulge configuration itself (shown in Figure 17d) can be unstable. Figure 20 gives in panels a–c three snapshots from the time evolution for $\overline{h} = 2.8$ with convective mobility $Q(h) = h^3$, while Figure 20d shows the evolution of the energy $F(t)$ for convective transport (red dashed line) and for surface diffusion (blue solid line). As in the previous cases, the evolution visits similar unstable steady states until a state with two bulges is formed. However, this time this state not only evolves via a coarsening event toward a single bulge, but at the same time forms a liquid bridge to the next MWS (the system is periodic in the x-direction). The final liquid bridge state is shown in Figure 20c. Notice that this final configuration is also observed in the experiments (see e.g., ref 46). However, the occurrence of this final configuration strongly depends on the domain size and periodicity of the wettability pattern. In the present paper, our setting focuses on periodic arrays of stripes at distances of the same order of magnitude as the stripe width itself. This allows us to study instabilities of single ridge solutions as well as to obtain liquid bridge states as final configuration. A detailed investigation of the influence of the distance between stripes on the dynamical behavior of the system requires an analysis of larger domains that involve several periods and would ideally incorporate continuation results for the 2d system. This aspect is not within the scope of the current study and will be pursued elsewhere.

5. CONCLUSION

We have employed a mesoscopic continuum model to analyze the redistribution stage of deposition experiments where organic molecules are deposited by vapor deposition on a solid substrate with stripe-like wettability patterns. In particular, we have investigated the stability of transversally invariant ridges located on the more wettable parts of a stripe pattern by means of a linear stability analysis of steady one-dimensional profiles that correspond to the transversally invariant ridges on two-dimensional substrates. Employing a technique based on continuation procedures has allowed us to perform the linear analysis very efficiently. In particular, we have studied the influence of the wettability contrast, the mean film thickness (ridge volume), and the geometry of the stripe pattern.

We have found that there exist two different instability modes that on the one hand result at large ridge volume in the formation of bulges that spill from the more wettable stripes onto the less wettable bare substrate and on the one hand result

DOI: 10.1021/acs.langmuir.5b02407
Langmuir 2015, 31, 10618–10631

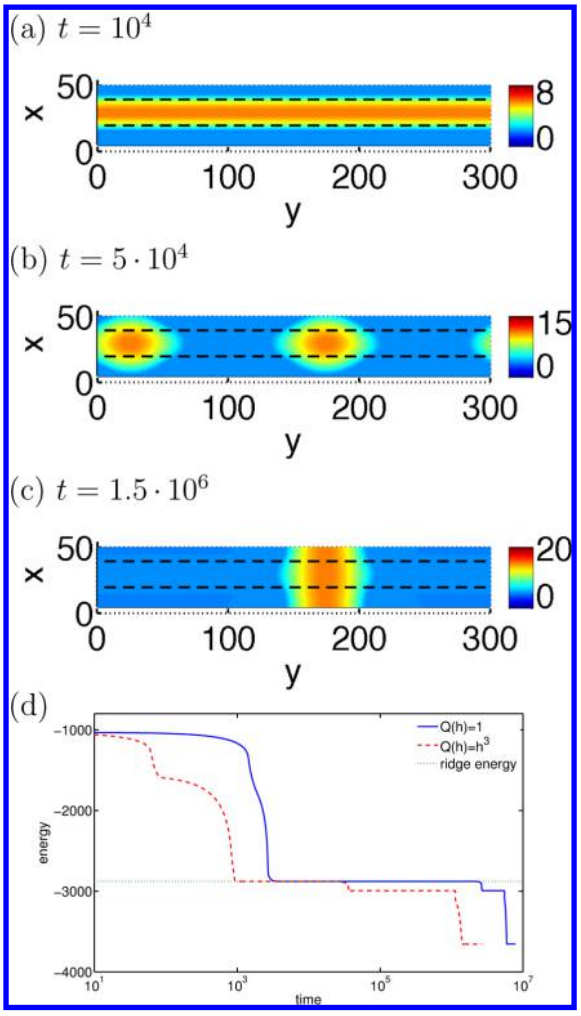

Figure 20. Snapshots from a direct time simulation of the thin film eq 1 with $\bar{h} = 2.8$, $l_s = 0.03$, $\rho = 0.5$, $x_A = 0.3$, and $L_{per} = 50$. Panels a, b, and c show snapshots at times $t = 10^4$, $t = 5 \times 10^4$, and $t = 1.5 \times 10^6$, respectively. The borders of the more wettable stripes (MWS) are indicated by dashed (black) lines. Panel d shows time series of the energy $F(t)$ for transport by surface diffusion (mobility $Q(h) \sim 1$, solid blue line) and by convection ($Q(h) \sim h^3$, dashed red line).

at small ridge volume in the formation of small droplets located on the more wettable stripes, respectively. The different modes are reflected in qualitatively different eigenmodes that have their maxima in the regions of the strongest wettability gradient and at the stripe center, respectively. They can be identified as a Rayleigh−Plateau instability and a surface instability as in spinodal dewetting, respectively.

In the parameter plane spanned by mean film height $\bar{h}$ (liquid volume) and wettability contrast ρ one sees that a clear distinction between the two modes appears at some wettability contrast ρ_c. For $\rho > \rho_c$ two unstable film thickness ranges exist with a stable range of film thicknesses in between. The critical ρ_c decreases with increasing steepness of the transition in wettability. In the opposite limit of a sinusoidal wettability pattern, i.e., when the transition zone is as wide as the period, no such distinction of two instability modes exists.

Further, we have investigated the role of the analyzed transversally invariant ridge states in the course of the fully nonlinear time evolution starting from a deposited homogeneous film of molecules toward the final bulge or drop geometry. This has allowed us to assess whether a detailed analysis of ridge stability is meaningful in the context of deposition experiments with striped substrates. We have found that even linearly unstable ridge states form the first 'organizing center' of the time evolution. This is because they (as well as all other unstable states) represent saddles in the state space of the system. One may say that they 'attract' time evolutions from the majority of directions in the infinite-dimensional space of system states and later 'expel' them into one or a few directions and with rates that both can be determined by a linear stability analysis of the unstable states. In particular, the evolution that starts at a flat film with small perturbations is first attracted by the ridge state (the corresponding time scale is related to both the most unstable eigenmode of the flat film and the slowest stable eigenmode of the ridge state). After approaching the transversally invariant ridge state, the evolution is expelled along the most unstable of the few unstable directions in state space. It corresponds to the most unstable eigenmode of the ridge state (the corresponding time scale is the inverse of the growth rate of this eigenmode). The importance of the ridge state and also of the other unstable states (as, e.g., multidrop states) for the time evolution can be clearly seen in the formation of 'energy plateaus' in all the plots that give the dependence of the free energy on time. Each plateau represents one of the unstable steady state. This observation is also important for other gradient dynamics systems, as it indicates how important it is to understand the *complete* solution structure of a system in order to control its time evolution. It is further expected that the unstable steady states are the ones that are most easily stabilized through imposed controls—be it spatial patterning, or feedback.

The conclusion in the previous paragraph is strengthened by our finding that the relevance of the unstable states holds for all the different dominant transport mechanisms that we have investigated: the same energy plateaus appear independently of the chosen mobility, however, we have found that their relative duration depends on the particular chosen transport behavior. This agrees with the fact discussed above that the steady states do not depend on mobilities, but that the time constants and eigenmodes do depend on them. As particular examples for the influence of the transport mechanism of redistribution on the evolution pathway, we have compared a standard long-wave hydrodynamic model in the case of no slip at the substrate (purely convective transport, cubic mobility) with diffusive transport via diffusion in the film bulk (linear mobility) and at the film surface (constant mobility). All the resulting long-wave evolution equations are gradient dynamics models on the identical underlying free energy (interface Hamiltonian) just with different mobility functions. As a result, one may now reconsider the film height evolution equation and combine thin film hydrodynamics for relatively thick layers and dynamical density functional theory for relatively thin layers by combining the corresponding mobilities.[72] This will allow one to investigate the crossover between different dominant transport mechanisms depending on various parameters.

Based on our investigations, we conclude more specifically that the different experimentally observed equilibrium morphologies do not result from the different transport mechanisms in the liquid or solid state as thought before. Instead, we have found that the observed flat and bulged deposits result from different balances of interface energies and wetting energies. The influence of bulk elastic energies may also play a role that shall be further investigated in the future.

DOI: 10.1021/acs.langmuir.5b02407
Langmuir 2015, 31, 10618−10631

■ ASSOCIATED CONTENT

Supporting Information

The Supporting Information is available free of charge on the ACS Publications website at DOI: 10.1021/acs.langmuir.5b02407.

(PDF)

■ AUTHOR INFORMATION

Corresponding Author

*Phone: +49-251-83-34939; E-mail: gurevics@uni-muenster.de.

Notes

The authors declare no competing financial interest.

■ ACKNOWLEDGMENTS

This work was partly supported by the Deutsche Forschungsgemeinschaft in the framework of the Sino-German Collaborative Research Centre TRR 61.

■ REFERENCES

(1) Evans, J.; Thiel, P.; Bartelt, M. Morphological evolution during epitaxial thin film growth: Formation of 2D islands and 3D mounds. **2006**, *61*, 1−128.

(2) Einax, M.; Dieterich, W.; Maass, P. Colloquium: Cluster growth on surfaces: Densities, size distributions, and morphologies. **2013**, *85*, 921−939.

(3) Wadley, H.; Zhou, A.; Johnson, R.; Neurock, M. Mechanisms, models and methods of vapor deposition. **2001**, *46*, 329−377.

(4) Siegert, M. Ordering dynamics of surfaces in molecular beam epitaxy. **1997**, *239*, 420−427.

(5) Mijatovic, D.; Eijkel, J. C. T.; van den Berg, A. Technologies for nanofluidic systems: Top-down vs. bottom-up - a review. **2005**, *5*, 492−500.

(6) Golovin, A.; Davis, S.; Voorhees, P. Self-organization of quantum dots in epitaxially strained solid films. **2003**, *68*, 056203.

(7) Korzec, M.; Evans, P. From bell shapes to pyramids: A reduced continuum model for self-assembled quantum dot growth. **2010**, *239*, 465−474.

(8) Wilson, S. K.; Hunt, R.; Duffy, B. R. The rate of spreading in spin coating. **2000**, *413*, 65−88.

(9) Schwartz, L. W.; Roy, R. V. Theoretical and numerical results for spin coating of viscous liquids. **2004**, *16*, 569−584.

(10) Reisfeld, B.; Bankoff, S.; Davis, S. The dynamics and stability of thin liquid-films during spin coating: 1. Films with constant rates of evaporation or absorption. **1991**, *70*, 5258−5266.

(11) Thiele, U.; Mertig, M.; Pompe, W. Dewetting of an evaporating thin liquid film: Heterogeneous nucleation and surface instability. **1998**, *80*, 2869−2872.

(12) Münch, A.; Please, C. P.; Wagner, B. Spin coating of an evaporating polymer solution. **2011**, *23*, 102101.

(13) Maenosono, S.; Okubo, T.; Yamaguchi, Y. Overview of nanoparticle array formation by wet coating. **2003**, *5*, 5−15.

(14) Thiele, U. Patterned deposition at moving contact line. **2014**, *206*, 399−413.

(15) Weinstein, S. J.; Ruschak, K. J. Coating flows. **2004**, *36*, 29−53.

(16) Oron, A.; Davis, S. H.; Bankoff, S. G. Long-scale evolution of thin liquid films. **1997**, *69*, 931−980.

(17) Wang, W.; Du, C.; Wang, C.; Hirtz, M.; Li, L.; Hao, J.; Wu, Q.; Lu, R.; Lu, N.; Wang, Y.; Fuchs, H.; Chi, L. High-Resolution Triple-Color Patterns Based on the Liquid Behavior of Organic Molecules. **2011**, *7*, 1403−1406.

(18) Wang, W.; Chi, L. Area-Selective Growth of Functional Molecular Architectures. **2012**, *45*, 1646−1656.

(19) Darhuber, A. A.; Troian, S. M.; Davis, J. M.; Miller, S. M.; Wagner, S. Selective dip-coating of chemically micropatterned surfaces. **2000**, *88*, 5119−5126.

(20) Berbezier, I.; Aouassa, M.; Ronda, A.; Favre, L.; Bollani, M.; Sordan, R.; Delobbe, A.; Sudraud, P. Ordered arrays of Si and Ge nanocrystals via dewetting of pre-patterned thin films. **2013**, *113*, 064908.

(21) Li, X.; Wang, C.; Yang, G. Thermodynamic theory of growth of nanostructures. **2014**, *64*, 121−199.

(22) Lenz, P.; Lipowsky, R. Morphological transitions of wetting layers on structured surfaces. **1998**, *80*, 1920−1923.

(23) Brusch, L.; Kühne, H.; Thiele, U.; Bär, M. Dewetting of thin films on heterogeneous substrates: Pinning vs. coarsening. **2002**, *66*, 011602.

(24) Thiele, U.; Brusch, L.; Bestehorn, M.; Bär, M. Modelling thin-film dewetting on structured substrates and templates: Bifurcation analysis and numerical simulations. **2003**, *11*, 255−271.

(25) Bauer, C.; Dietrich, S.; Parry, A. O. Morphological phase transitions of thin fluid films on chemically structured substrates. **1999**, *47*, 474−480.

(26) Bauer, C.; Dietrich, S. Phase diagram for morphological transitions of wetting films on chemically structured substrates. **2000**, *61*, 1664−1669.

(27) Moosavi, A.; Rauscher, A.; Dietrich, S. Motion of nanodroplets near chemical heterogeneities. **2008**, *24*, 734−742.

(28) Beltrame, P.; Knobloch, E.; Hänggi, P.; Thiele, U. Rayleigh and depinning instabilities of forced liquid ridges on heterogeneous substrates. **2011**, *83*, 016305.

(29) Mechkov, S.; Rauscher, M.; Dietrich, S. Stability of liquid ridges on chemical micro- and nanostripes. **2008**, *77*, 061605.

(30) Kargupta, K.; Konnur, R.; Sharma, A. Instability and pattern formation in thin liquid films on chemically heterogeneous substrates. **2000**, *16*, 10243−10253.

(31) Kargupta, K.; Sharma, A. Templating of thin films induced by dewetting on patterned surfaces. **2001**, *86*, 4536−4539.

(32) Kargupta, K.; Sharma, A. Mesopatterning of thin liquid films by templating on chemically patterned complex substrates. **2003**, *19*, 5153−5163.

(33) Vellingiri, R.; Savva, N.; Kalliadasis, S. Droplet spreading on chemically heterogeneous substrates. **2011**, *84*, 036305.

(34) Brinkmann, M.; Lipowsky, R. Wetting morphologies on substrates with striped surface domains. **2002**, *92*, 4296−4306.

(35) Brinkmann, M.; Kierfeld, J.; Lipowsky, R. Stability of liquid channels or filaments in the presence of line tension. **2005**, *17*, 2349−2364.

(36) Seemann, R.; Brinkmann, M.; Kramer, E. J.; Lange, F. F.; Lipowsky, R. Wetting morphologies at microstructured surfaces. **2005**, *102*, 1848−1852.

(37) Sehgal, A.; Ferreiro, V.; Douglas, J. F.; Amis, E. J.; Karim, A. Pattern-directed dewetting of ultrathin polymer films. **2002**, *18*, 7041−7048.

(38) Checco, A.; Ocko, B.; Tasinkevych, M.; Dietrich, S. Stability of Thin Wetting Films on Chemically Nanostructured Surfaces. **2012**, *109*, 166101.

(39) Gau, H.; Herminghaus, S.; Lenz, P.; Lipowsky, R. Liquid morphologies on structured surfaces: From microchannels to microchips. **1999**, *283*, 46−49.

(40) Herminghaus, S.; Brinkmann, M.; Seemann, R. Wetting and dewetting of complex surface geometries. **2008**, *38*, 101−121.

(41) Srolovitz, D. J.; Safran, S. A. Capillary instabilities in thin films. II. **1986**, *60*, 255−260.

DOI: 10.1021/acs.langmuir.5b02407
Langmuir 2015, 31, 10618−10631

(42) Misbah, C.; Pierre-Louis, O.; Saito, Y. Crystal surfaces in and out of equilibrium: A modern view. . **2010**, *82*, 981−1040.
(43) Archer, A. J.; Robbins, M. J.; Thiele, U. Dynamical density functional theory for the dewetting of evaporating thin films of nanoparticle suspensions exhibiting pattern formation. **2010**, *81*, 021602.
(44) Münch, A.; Wagner, B.; Witelski, T. P. Lubrication models with small to large slip lengths. . **2005**, *53*, 359−383.
(45) Thiele, U. Thin film evolution equations from (evaporating) dewetting liquid layers to epitaxial growth. **2010**, *22*, 084019.
(46) Wang, W.; Du, C.; Li, L.; Wang, H.; Wang, C.; Wang, Y.; Fuchs, H.; Chi, L. Addressable Organic Structure by Anisotropic Wetting. . **2013**, *25*, 2018−2023.
(47) Lied, F.; Mues, T.; Wang, W.; Chi, L.; Heuer, A. Different growth regimes on prepatterned surfaces: Consistent evidence from simulations and experiments. . **2012**, *136*, 024704.
(48) de Gennes, P.-G. Wetting: Statics and dynamics. . **1985**, *57*, 827−863.
(49) Starov, V. M.; Velarde, M. G. Surface forces and wetting phenomena. **2009**, *21*, 464121.
(50) Craster, R. V.; Matar, O. K. Dynamics and stability of thin liquid films. . **2009**, *81*, 1131−1198.
(51) Krauskopf, B., Osinga, H. M., Galan-Vioque, J., Eds. Springer: Dordrecht, 2007.
(52) Dijkstra, H. A.; Wubs, F. W.; Cliffe, A. K.; Doedel, E.; Dragomirescu, I. F.; Eckhardt, B.; Gelfgat, A. Y.; Hazel, A.; Lucarini, V.; Salinger, A. G.; Phipps, E. T.; Sanchez-Umbria, J.; Schuttelaars, H.; Tuckerman, L. S.; Thiele, U. Numerical Bifurcation Methods and their Application to Fluid Dynamics: Analysis beyond Simulation. *Commun. Comput. Phys.* **2014**, *15*, 1−45.
(53) Thiele, U. *Münsteranian Torturials: LINDROP - Linear stability of steady solutions of a thin film equation for a horizontal homogeneous substrate*, 2015; http://www.uni-muenster.de/CeNoS/Lehre/Tutorials.
(54) Kalliadasis, S., Thiele, U., Eds. Springer: Wien/New York, 2007; CISM 490..
(55) Israelachvili, J. N. , 3rd ed.; Academic Press: London, 2011.
(56) Pismen, L. M. Mesoscopic hydrodynamics of contact line motion. **2002**, *206*, 11−30.
(57) The film height is scaled by $d = \left(\frac{B}{A}\right)^{1/3}$, the x and y coordinates by $L = \sqrt{\frac{\gamma}{A}}d^2$, the effective interface potential by $\kappa = \frac{A}{d^2}$, and the time by $\tau = \frac{3\eta L^2}{\kappa d}$.
(58) Bonn, D.; Eggers, J.; Indekeu, J.; Meunier, J.; Rolley, E. Wetting and spreading. . **2009**, *81*, 739−805.
(59) Mitlin, V. S. Dewetting of Solid Surface: Analogy with Spinodal Decomposition. . **1993**, *156*, 491−497.
(60) Cahn, J. W. Phase separation by spinodal decomposition in isotropic systems. . **1965**, *42*, 93−99.
(61) MacDowell, L.; Benet, J.; Katcho, N.; Palanco, J. Disjoining pressure and the film-height-dependent surface tension of thin liquid films: New insight from capillary wave fluctuations. . **2014**, *206*, 150−171.
(62) Archer, A. J.; Rauscher, M. Dynamical density functional theory for interacting Brownian particles: Stochastic or deterministic? . **2004**, *37*, 9325−9333.
(63) Yochelis, A.; Knobloch, E.; Pismen, L. M. Formation and mobility of droplets on composite layered substrates. . **2007**, *22*, 41−49.
(64) Cueto-Felgueroso, L.; Juanes, R. Stability analysis of a phase-field model of gravity-driven unsaturated flow through porous media. **2009**, *79*, 036301.
(65) Doedel, E.; Keller, H. B.; Kernevez, J. P. Numerical analysis and control of bifurcation problems (I) Bifurcation in finite dimensions. . **1991**, *1*, 493−520.
(66) Doedel, E. J.; Oldeman, B. E. *AUTO07p: Continuation and Bifurcation Software for Ordinary Differential Equations*; Concordia University: Montreal, 2009.
(67) Thiele, U., Kamps, O., Gurevich, S. V., Eds. *Münsteranian Torturials on Nonlinear Science: Continuation*; CeNoS: Münster, 2014; http://www.uni-muenster.de/CeNoS/Lehre/Tutorials.
(68) Brochard-Wyart, F.; Redon, C. Dynamics of liquid rim instabilities. **1992**, *8*, 2324−2329.
(69) Thiele, U.; Knobloch, E. Front and back instability of a liquid film on a slightly inclined plate. **2003**, *15*, 892−907.
(70) Witelski, T. P.; Bowen, M. ADI Schemes for Higher-order Nonlinear Diffusion Equations. . **2003**, *45*, 331−351.
(71) Lin, T.; Kondic, L.; Filippov, A. Thin films flowing down inverted substrates: Three-dimensional flow. **2012**, *24*, 022105.
(72) In the context of diffusion one may prefer to write the gradient dynamics in terms of adsorption Γ instead of film height h. For constant and homogeneous liquid density ρ_l they are related by $\Gamma = \rho_l h$. For a discussion of the relation in the context of determining wetting energies from a lattice gas density functional theory, see ref 73.
(73) Hughes, A. P.; Thiele, U.; Archer, A. J. Liquid drops on a surface: using density functional theory to calculate the binding potential and drop profiles and comparing with results from mesoscopic modelling. . **2015**, *142*, 074702.

DOI: 10.1021/acs.langmuir.5b02407
Langmuir 2015, 31, 10618−10631